Interferometric mapping of material properties using thermal perturbation

Georges Goetz[a,b,1,2], Tong Ling[a,c,1,2], Tushar Gupta[d], Seungbum Kang[e], Jenny Wang[a,f], Patrick D. Gregory[g], B. Hyle Park[g], and Daniel Palanker[a,c,2]

[a]Hansen Experimental Physics Laboratory, Stanford University, Stanford, CA 94305; [b]Department of Neurosurgery, Stanford University, Stanford, CA 94305; [c]Department of Ophthalmology, Stanford University, Stanford, CA 94305; [d]Department of Electrical Engineering, Stanford University, Stanford, CA 94305; [e]Department of Ophthalmology and Visual Science, The Catholic University of Korea, Seoul 06591, Republic of Korea; [f]Department of Applied Physics, Stanford University, Stanford, CA 94305; and [g]Department of Bioengineering, University of California, Riverside, CA 92521

Edited by David R. Williams, University of Rochester, Rochester, NY, and approved January 31, 2018 (received for review July 17, 2017)

Optical phase changes induced by transient perturbations provide a sensitive measure of material properties. We demonstrate the high sensitivity and speed of such methods, using two interferometric techniques: quantitative phase imaging (QPI) in transmission and phase-resolved optical coherence tomography (OCT) in reflection. Shot-noise–limited QPI can resolve energy deposition of about 3.4 mJ/cm^2 in a single pulse, which corresponds to 0.8 °C temperature rise in a single cell. OCT can detect deposition of 24 mJ/cm^2 energy between two scattering interfaces producing signals with about 30-dB signal-to-noise ratio (SNR), and 4.7 mJ/cm^2 when SNR is 45 dB. Both techniques can image thermal changes within the thermal confinement time, which enables accurate single-shot mapping of absorption coefficients even in highly scattering samples, as well as electrical conductivity and many other material properties in biological samples at cellular scale. Integration of the phase changes along the beam path helps increase sensitivity, and the signal relaxation time reveals the size of hidden objects. These methods may enable multiple applications, ranging from temperature-controlled retinal laser therapy or gene expression to mapping electric current density and characterization of semiconductor devices with rapid pump–probe measurements.

quantitative phase imaging | optical coherence tomography | imaging | finite-element modeling | retinal laser therapy

Transient perturbation of samples is a popular technique for nondestructive characterization of materials (1–3). It enables detection of cavities or other subsurface defects (4), evaluation of composite repairs (5), or analysis of the function and failure modes of integrated circuits (6). Similarly, in medicine, real-time assessment of energy deposition in tissue and control of the associated temperature rise has many applications, ranging from temperature-controlled gene expression for tumor inhibition in oncology (7) to retinal laser therapy in ophthalmology (8, 9).

Optical imaging techniques can be very sensitive to small variations in material properties, and they have been used with great success for detecting local deviations from the average properties of the material. For example, tomographic imaging of changes in temperature (4), emissivity (10), and thermo-transmittance (11) can reveal subsurface features, such as holes or discontinuities. Photoluminescent spectroscopy can map dopant concentrations in semiconductors (12). Interferometric detection of tissue surface motion can reveal the dynamics of thermally induced waves (13) and the onset of photocoagulation in the living eye (9). Phase-sensitive optical coherence tomography (OCT) can detect changes in optical path length caused by heating of water under repetitive pulsing (14–16). Similarly, photothermal microscopy is based on inducing small changes in refraction or scattering by periodic heating with a tightly focused laser beam and detecting them using lock-in amplification (17, 18). Since this technique is based on slow signal integration and point-by-point scanning, it is not suitable for simultaneous imaging of a large field or mapping sample dynamics, unlike single-shot full-field interferometric techniques like quantitative phase imaging (QPI) (19–25).

Distinguishing between absorption and scattering in attenuation measurements is a significant challenge, especially for biological samples (26, 27). For samples with relatively low absorption, integrating cavity spectroscopy offers a solution, especially when combined with ring-down spectroscopy (28). Measuring the absorption coefficient in a nearly opaque sample, where no photons reach the detector, remains challenging. Interferometric techniques using a wavelength at which absorption is low to probe thermal changes induced by the laser at the wavelength of interest offer a unique solution to both problems.

In this paper, we demonstrate rapid, accurate, and nondestructive measurements of material properties by two interferometric techniques: QPI in transmission and phase-resolved OCT in reflection. Imaging the heat-induced changes in refractive index using wide-field diffraction phase microscopy (QPI) can quantitatively map the optical absorption, the distribution of electric field in a conductive material, or the energy deposition pattern from another source. Similarly, phase-resolved OCT can detect variations of the absorption coefficient in multilayered

Significance

Rapid, accurate, and nondestructive mapping of material properties is of great interest in many fields, with applications ranging from detection of defects or other subsurface features in semiconductors to estimating temperature rise in various tissue layers during laser therapy. We demonstrate the speed and precision of two interferometric techniques, quantitative phase imaging and phase-resolved optical coherence tomography, in recording optical phase changes induced by energy deposition in various materials. Such phase perturbations can be used to infer sample properties, ranging from absorption and temperature maps to distribution of electric field or resistivity. We derive the theoretical sensitivity limits of such techniques and demonstrate their applicability to the mapping of absorption coefficients, temperature, and electric fields in synthetic and biological samples.

Author contributions: G.G., T.L., and D.P. designed research; G.G., T.L., T.G., and S.K. performed experiments; T.L. and J.W. performed computational modeling; P.D.G. and B.H.P. designed and assembled the OCT system; G.G. and T.L. analyzed data; and G.G., T.L., and D.P. wrote the paper.

The authors declare no conflict of interest.

This article is a PNAS Direct Submission.

[1]G.G. and T.L. contributed equally to this work.

[2]To whom correspondence may be addressed. Email: ggoetz@alumni.stanford.edu, tongling@stanford.edu, or palanker@stanford.edu.

This article contains supporting information online at www.pnas.org/lookup/suppl/doi:10.1073/pnas.1712763115/-/DCSupplemental.

Published online February 26, 2018.

structures based on heat-induced material expansion. While we demonstrate these techniques using pulsed heating, materials could also be perturbed by electric and magnetic fields, ultrasound, and other sources of stress. Both imaging modalities exhibit high sensitivity and spatial and temporal resolution. QPI can detect microjoule energy deposition into single biological cells with temporal resolution limited only by the imaging flash duration—microseconds and even shorter. Phase-resolved OCT can monitor changes in retinal temperature at 100 kHz, with subkelvin accuracy. With both techniques, the time course of stress relaxation is indicative of the size of the heated object, which might enable characterization of objects hidden in the bulk.

Sensitivity of Interferometric Calorimetry

Interferometric measurements of perturbation-induced changes in the optical pathway can provide insight into optical and mechanical properties of the samples under study. We derive the theoretical sensitivity limits of QPI and phase-resolved OCT for measuring material properties and then demonstrate the capabilities of these techniques through experimental measurements based on transient heating of synthetic and biological samples. While we use thermal perturbations both in our theoretical derivations and in experimental demonstrations, the approach can be extended to other kinds of perturbation, such as deformations by electric or magnetic fields, ultrasonic pressure waves, and others.

In the shot-noise–limited regime, the phase sensitivity ϕ_s of both QPI and OCT can be written as (14, 29, 30)

$$\delta^2\phi_s = \frac{1}{\eta N}, \qquad [1]$$

where N denotes the total number of photons incident on each pixel of the camera for QPI and spectral-domain OCT, or photons incident on the balanced detector for swept-source OCT, and η is the quantum efficiency of the camera or detector at the wavelength of interest.

In a linear approximation, small changes in refractive index induced by the temperature rise resulting from thermal perturbation can be estimated as $\delta n \simeq \alpha \cdot \delta T$. The change in the optical phase accumulated along the imaging beam path between two points of interest can then be written as

$$\delta\phi = \frac{2\pi}{\lambda}\int \alpha \cdot \delta T dx. \qquad [2]$$

With the local temperature rise δT being proportional to the deposited energy density ϵ divided by the material density ρ and its volumetric heat capacity c_v,

$$\delta T = \frac{\epsilon}{\rho c_v}. \qquad [3]$$

Integration along the path yields

$$\delta\phi = \alpha\frac{2\pi}{\lambda}\frac{E}{\rho c_v}, \qquad [4]$$

where E is the total energy deposited in the material between the two points of interest along the imaging path per unit area of the probing beam. This derivation assumes that the measurement occurs within the thermal confinement time, i.e., before the heat diffuses away from the absorption area. Sensitivity of the system can be similarly derived based on the thermal expansion coefficient or other types of deformation affecting the optical path.

The perturbation-induced phase change $\delta\phi$ can be used directly to infer some material properties, for example the absorption coefficient of a sample. The amount of energy absorbed in a scattering sample with absorption coefficient μ and thickness L is $E_i(1 - e^{-\mu L})$, with E_i denoting the incident energy per unit area. If the energy is not totally absorbed, the absorption coefficient can be derived from the phase change as follows:

$$\mu = -\frac{1}{L}\ln\left(1 - \frac{\lambda\rho c_v\delta\phi}{2\pi\alpha E_i}\right). \qquad [5]$$

One advantage of such a measurement is that the phase change is induced only by the absorbed photons, distinguishing it from the beam attenuation due to scattering. Furthermore, using a longer wavelength to probe the phase signal without attenuation, the measurement noise does not depend on absorption, while in conventional measurement of transmitted power, noise increases with stronger absorption due to loss of photons.

To maximize precision while avoiding sample damage, the measurement can be performed in two steps. An initial measurement at low energy will define an approximate value of the absorption coefficient. Then the pulse energy E_i can be increased to induce a temperature rise $\Delta T = \mu E_i/(\rho c_v)$ just below the damage threshold, thereby maximizing the phase change and the associated signal-to-noise ratio (SNR) of the measurement. Since heat diffusion during the measurement smears the temperature distribution, heating and imaging performed within the thermal confinement time will provide more accurate mapping of the absorption coefficient.

Experimentally, our QPI microscope and OCT system both exhibited phase noise close to their theoretical shot-noise limit. Our effective electron well depth in QPI was approximately 4,200 electrons, as imbalances between the sample and the reference arms prevented dark fringes from reaching zero count, which reduced the well depth from the full 11,000 provided by the camera. As Gaussian filtering during phase reconstruction blurred the image over approximately 7 pixels, with 4.6 pixels sampling each fringe, the theoretical noise limit was 5.2 mrad, which compares favorably with the 5.8-mrad noise measured. In water at room temperature, $\alpha = 0.9 \times 10^{-4}$ K^{-1}, $c_v = 4.19$ $J{\cdot}K^{-1}{\cdot}g^{-1}$, and $\rho = 1$ $g{\cdot}cm^{-3}$. Therefore, the QPI microscope with its 5.8-mrad noise level is sensitive to deposition of 3.4 $mJ{\cdot}cm^{-2}$ in a sample. This corresponds to deposition of 2.7 nJ of energy in a 10-μm diameter cell, which leads to heating by about 0.82 °C, and a temperature rise of 2.5 °C can be detected at the 3σ level.

With OCT, we measured a phase noise of 41.3 mrad rms between two interfaces, with an SNR of 27.6 and 31 dB (the corresponding theoretical limit of phase stability is 41.7 mrad). Between two such interfaces, phase-resolved OCT can therefore detect refractive index changes induced by deposition of approximately 24 mJ/cm^2. For a 40-μm diameter probing beam, deposition of 0.30 μJ can therefore be detected at the 3σ rms noise level. If all this energy is absorbed in a 10-μm–thick layer, it will increase the tissue temperature by 5.7 °C. Monitoring the changes in a thicker layer of the uniformly heated tissue, including not only the retinal pigment epithelium (RPE) but also the retina and choroid, improves sensitivity in proportion to the layer thickness. For example, with a 100-μm–thick layer, the threshold corresponds to an average temperature rise of 0.57 °C. As thermal expansion dominates the phase changes measured with biological tissues in reflection and leads to signals approximately three times larger than expected from a purely refractive index change (9), OCT sensitivity to energy deposition is actually three times better than the above estimate and similar to that of QPI.

High-Speed Imaging of Energy Deposition with QPI

To demonstrate the speed and accuracy in measurement of energy deposition with QPI, we painted a thin (<10 μm) red film on a glass slide, immersed it in distilled water, and illuminated it with a 1.1-ms pulse at 450-nm wavelength (*Materials*

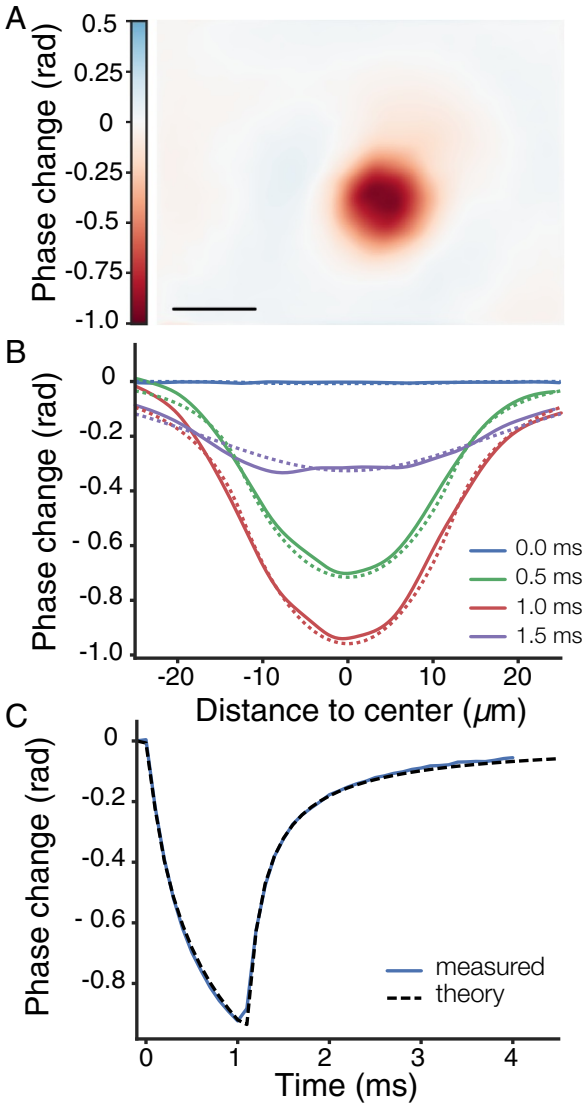

Fig. 1. QPI of the heating of a thin absorptive layer. (*A*) Phase change at the end of a 1.1-ms–long pulse of 11 mW peak power, focused into a 25-μm spot on an absorptive film. (Scale bar: 25 μm.) (*B*) Radial profile of the phase change at various time points (t = 0 is the beginning of the heating pulse). Solid lines, experimental measurements; dashed lines, computational modeling. (*C*) Phase signal in the center of the heating beam over time: experimental and computed data.

and Methods). A 25-μm spot was illuminated with a peak power of 11 mW, as shown in Fig. 1*A*, while the sample was imaged at 10 kfps over a 133×99-μm^2 area. To check whether the water index change with temperature accounts for the phase changes observed, we modeled the experimental settings using COMSOL 5.2a, as described in *Materials and Methods*. As shown in Fig. 1 *B* and *C*, experimental measurements and theoretical predictions were in excellent agreement, in terms of both spatial and temporal evolution of the phase change, with only 4.5 ± 11.6 mrad (mean ± SD) difference, on average, between the theory and measurement of the time course. Temperature had risen by 93 K at the end of the 1-ms pulse, corresponding to a −0.92 rad maximum change in optical phase. Within approximately 1 ms after the end of the pulse, heat diffused away, and the phase relaxed back to its original value. Movie S1 shows the spatiotemporal evolution of the optical phase during and after the heating pulse.

Energy absorbed by the red film was retrieved from this measurement by minimizing the difference between the model and experimental data, using a general optimization method based on gradient descent (*Materials and Methods*). As a result, a transmittance of 37.92 ± 0.08% (mean ± SD) was obtained—very close to the 40% value obtained with a power meter.

Joule heating of a conductive medium by electric current injected via a 6.4-μm inner diameter micropipette resulted in a phase change exceeding 1 rad, as shown in Fig. 2*D*. We delivered a 20-μs–long, 0.9-mA square pulse of current through the 40-kΩ impedance pipette and modeled the corresponding Joule heating (*Materials and Methods* and Fig. 2 *A*–*C*). At the end of the pulse, the water temperature rose by 120 K, resulting in a maximum phase change of 1.22 rad in good agreement between the model and the measurements (Fig. 2). The current retrieved by minimizing the difference between the model and these measurements yielded a value only 1.7% above the experimental setting.

Measuring Absorption with Phase-Resolved OCT

To image temperature-induced changes in stained water and to measure its absorption coefficient with phase-sensitive OCT, we used a 1-mm–thin layer of water stained with a red dye, confined between two glass coverslips (*Materials and Methods*). The sample was illuminated with a 2-ms pulse of blue laser (450 nm) at 400 mW peak power, focused into a 254-μm diameter spot (Fig. 3*A*). The sample was left open on the sides to allow for water expansion. An OCT beam of 40 μm in diameter was propagating collinear with the blue beam, and its reflection from the two glass slides was collected back into the sample arm (Fig. 3*C*). Changes in the optical path length between the glass slides revealed two distinct phenomena, as shown in Fig. 3*C*. Heating of water resulted in a decrease of its optical thickness due to the decrease of its refractive index (left vertical axis). Heat diffusing into the glass resulted in its thermal expansion, leading to an increase in the optical path between its surfaces (right vertical axis). Finite-element modeling of the refractive change in water and expansion of glass with heating matched the experimental results very closely, as shown in Fig. 3*C*. The maximum temperature rise in the sample at the end of the heating pulse was 59 °C.

An absorption coefficient of 52.3 ± 0.11 mm^{-1} was retrieved by fitting the phase change in the finite-element modeling (FEM) model to experimental measurement, which closely matched the 49.4-mm^{-1} value obtained from the measurement of transmitted power. Interestingly, we had to reduce the concentration of the dye (Alizarin Red S) nearly 50 times in the latter measurement to allow transmission of about half of the incident light for a precise power measurement.

In the second inorganic sample, blue light was absorbed in a thin (<10 μm) layer of red polymer painted onto frosted glass (68% absorption at 450 nm), placed at the bottom of a cuvette filled with water. A plastic coverslip located 200 μm above the top surface of the frosted glass provided a reference optical surface for the OCT measurement. The sides of the cuvette were left open to allow for water expansion during heating. A 1-ms–long, 150-mW pulse of 450 nm laser light was applied to a 250-μm spot on the red film. The decrease in the optical phase of the beam reflected from the surface of the red film was caused by two phenomena: a decrease in the refractive index of water and expansion of the red film. Modeling of the water component demonstrated that it accounted for about one-third of the total measured phase change, as illustrated in Fig. 3*D*. For materials with large thermal expansion coefficients, such as polymers or biological tissue [the linear expansion coefficient of polyethylene is typically 2×10^{-4} K^{-1}, compared with 7×10^{-5} K^{-1} for water (31)], mechanical expansion of the sample dominates the phase change observed during heating.

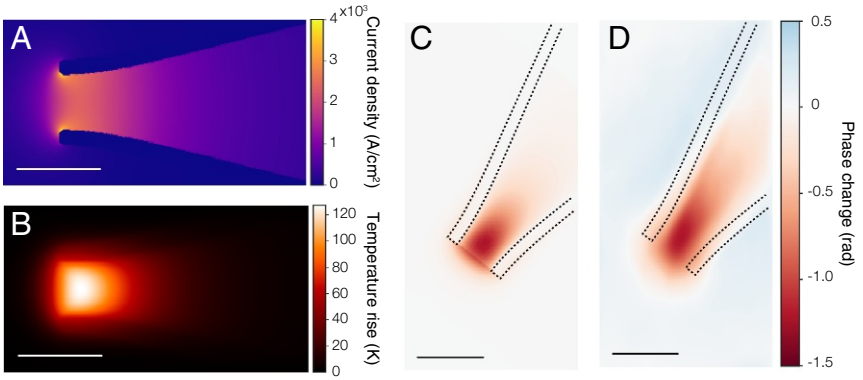

Fig. 2. QPI of Joule heating in electrolyte. (*A*) Density of electric currents delivered via a glass pipette of 6.4 μm inner diameter (computational modeling). (*B*) Temperature at the end of the 20-μs pulse. (*C*) Calculated phase change at the end of the heating pulse, with its maximum of −1.24 rad. (*D*) Experimental QPI map with a maximum phase change of −1.22 rad at the end of the electrical pulse. (Scale bars: 10 μm.)

Estimating the Temperature Rise of RPE with Phase-Resolved OCT

Measurements of the heat-induced phase changes in RPE and choroid could enable monitoring temperature rise during retinal laser therapy. In turn, this could help titrate the laser power or exposure duration to deliver a proper dose in each treatment spot, despite variations in tissue pigmentation or in ocular transparency between different areas in the eye (32). To assess the heat-induced changes in tissue with OCT, we applied a heating laser pulse to an eyecup preparation, which included RPE, choroid, and sclera. The neural retina was removed to reduce the likelihood of measuring changes due to photoreceptors bleaching (33) and to their gradual opacification ex vivo. The 450-nm laser beam was focused onto a 200-μm diameter spot on the RPE. Using a voltage-controlled tip–tilt mirror, 16 spots (4 × 4 grid) were applied at the same power, separated by 211 μm and 273 μm in *x* and *y* directions of the grid, respectively (*Materials and Methods*).

A phase change as large as 8 rad was detected from the RPE at the end of a 1-ms pulse at 250 mW peak power, with nearly constant slope during the heating phase (Fig. 4*A*). Fig. 4*B* shows the OCT A-scan (amplitude of scattering in tissue) and the corresponding phase change rate at various depths. The phase signal is not plotted in the areas of low scattering due to insufficient SNR. To extract the maximum phase change rate, we calculated the intensity-weighted average of the phase signal, similar to the methodology used in Doppler OCT (34), over a 30-μm depth range, within 150 μm from the top surface. The 30-μm range was

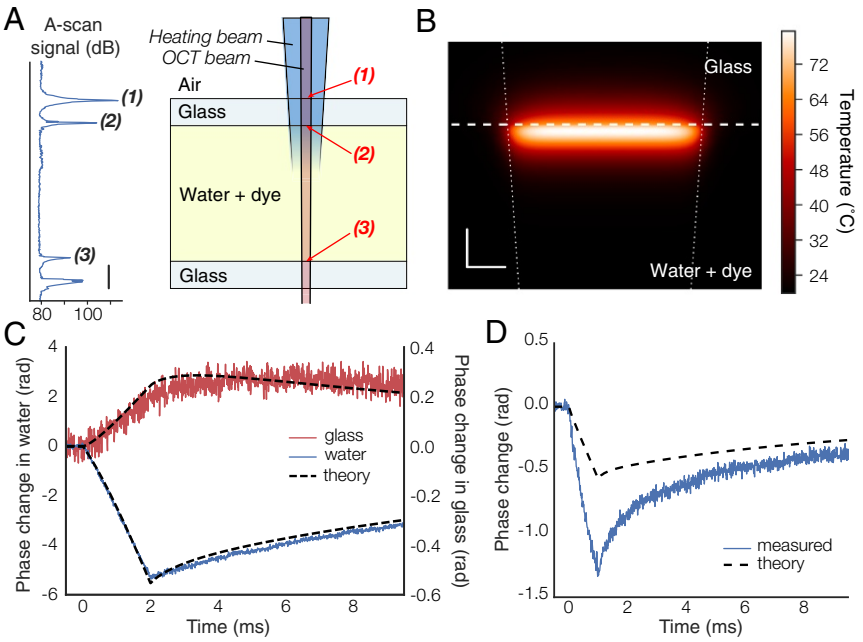

Fig. 3. OCT measurements of heat-induced phase changes. (*A*) Stained water between two glass coverslips is heated by the blue beam. A collinear OCT probe measures the phase changes between the peaks in the A-scan. (Scale bar: 200 μm.) (*B*) Computational modeling of the temperature distribution at the end of the 400-mW, 2-ms–long pulse. (Scale bars: 50 μm.) (*C*) Changes in the optical path length within the glass slide (between points *1* and *2* in the A-scan) match the thermal expansion of the glass. Phase changes in the liquid (between points *2* and *3*) match the calculations based on the temperature dependence of the refractive index of water. (*D*) A plastic film on the glass slide at the bottom of the chamber filled with water is heated by a laser. The measured phase change is much larger than can be accounted for from the decrease in refractive index of water (dashed black line). The rest of the signal is due to expansion of the film.

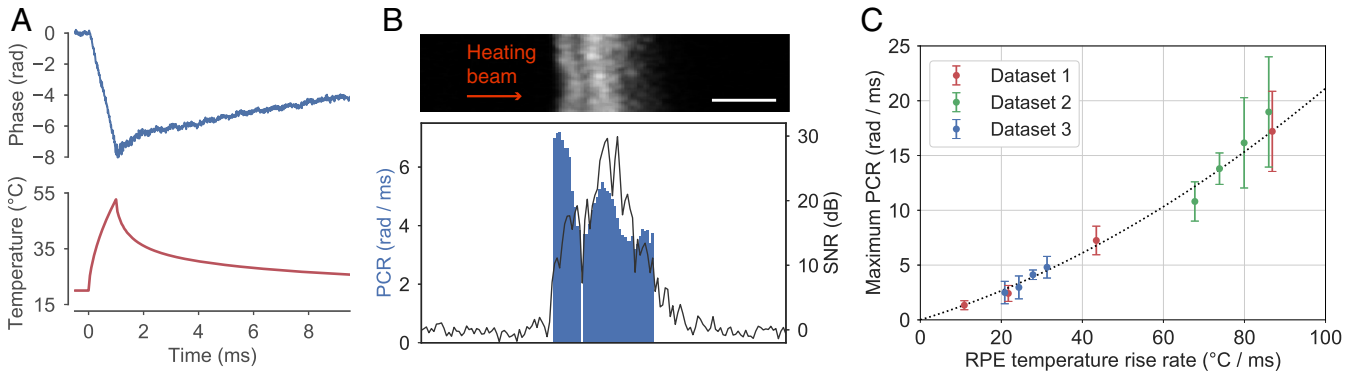

Fig. 4. Monitoring of the energy absorption in pigmented ocular tissues (RPE and choroid) with phase-resolved OCT. (*A*) Phase change and temperature rise on RPE surface induced by a 1-ms, 250-mW laser pulse. (*B*, *Top*) B-scan of the rat eyecup, including the RPE, choroid, and sclera. (Scale bar: 100 μm.) (*B*, *Bottom*) The phase change rate (PCR) at various depths of an A-scan. (*C*) Maximum PCR as a function of temperature rise rate. Each color represents an independent dataset from different eyes. Error bars represent the SD of the measurements from each 4 × 4 grid. The dashed curve represents a quadratic fit to the data with the equation $s = 0.116p + 9.43 \times 10^{-4}p^2$.

selected because it corresponds to the heat diffusion length for a 1-ms exposure, which essentially averages the heat distribution in tissue. The maximum phase change rate exhibited good reproducibility not only over the spots in each 4 × 4 grid, but also between the samples from different animals.

The RPE temperature calculated using a FEM model of retinal heating (*Materials and Methods*) for the 250-mW, 1-ms pulse is shown in Fig. 4*A*. Time course of the temperature is very different from that of the optical phase because the total phase change is defined primarily by the amount of energy captured along the OCT beam path, and only radial diffusion taking the energy away from the axis can affect it. With a 200-μm diameter beam, the radial diffusion time constant is on the order of 10 ms. The temperature course, however, is also affected by the much faster axial diffusion from the RPE, and the characteristic relaxation time is similar to the duration of the heating pulse—1 ms.

Plotting the maximum phase change rate against the temperature rise rate at various power levels (Fig. 4*C*) reveals a nonlinear relation, likely due to the faster than linear increase of the expansion coefficient with temperature (31). Importantly for practical applications, the same curve fits all three datasets taken on the samples from different animals.

Inferring the Shape of Hidden Objects from the Time Course of the Phase Response

When transient heating is applied to an object embedded in a different material, heat diffusion affects the time course of the thermal response, especially its thermal relaxation. This signature can be used to infer the size of the hidden objects without resolving them with an imaging system. Two examples of such analysis are shown in Fig. 5. For very shallow heating (penetration depth smaller than the beam diameter, Fig. 5 *A* and *B*) in a system consisting of water and glass, diffusion is predominantly axial. Since the refractive index of water varies with temperature much more than that of glass, diffusion of heat from water into glass reduces the phase change. Two features make the phase time course dependent on the absorption coefficient in this case: (*i*) Even if all of the energy is absorbed, amplitude of the phase change at the end of the heating pulse is increasing with stronger absorption due to faster than linear dependence of refractive index on temperature. (*ii*) Shallower penetration results in faster relaxation. Both features enable extracting the absorption coefficient from the phase measurement even in a completely opaque sample, when no transmitted power can be measured.

In the case of a long cylindrical sample (Fig. 5*C*), the relaxation time is defined by the radial heat diffusion. As shown in Fig. 5*D*, this feature allows extracting the sample diameter since the narrower the cylinder is, the faster it cools down.

Discussion

We demonstrated a highly sensitive approach for characterizing materials based on interferometric detection of rapid changes induced by transient perturbations of a sample. The two quantitative phase-sensitive techniques we used, QPI (35) and phase-resolved OCT (14, 15), have similar theoretical limits of sensitivity in the shot-noise–limited regime and can both provide high temporal resolution (10 kHz and above). QPI enables wide-field imaging at the expense of depth resolution, whereas OCT provides depth-resolved information, but typically requires lateral scanning to acquire a full volume. Since OCT uses back-reflected photons, its sensitivity is reduced in applications where boundaries between materials have very similar refractive indexes, such as biological cells in tissue, for example.

Imaging heat-induced changes in refractive index allows for precise characterization and monitoring of samples. QPI is sensitive to deposition of 10 nJ in cell-sized areas, which corresponds to a subdegree temperature increase in single cells with microsecond-range time resolution. This could be used for temperature monitoring in cell cultures for applications such as heat-induced control of gene expression (7). Measuring stress-induced changes in materials can also be used to infer properties such as thermal expansion or absorption coefficients. Determining absorption coefficients of biological samples is generally of significant diagnostic and therapeutic interest, but with traditional techniques based on transmission measurements, scattering in the sample often obscures the absorption spectrum. Distinguishing between the scattering- and absorption-induced beam attenuation is generally a difficult problem (26–28). As heating results from only the absorbed energy, interferometric detection of heating in the sample allows precise measurements of the absorption coefficient, even in nearly opaque samples.

For determination of the expansion coefficient, OCT is more sensitive than QPI since it directly detects the boundary movement in reflection, while QPI detects much smaller difference in optical path length determined by the product of the boundary displacement and the difference in refractive indexes across the boundary. In addition, since QPI integrates phase changes along the focal depth of the probing beam, expansion of a thin film is partially offset by the associated decrease in refractive index of the material. Therefore, with OCT, thermal expansion of the material becomes the dominant factor for most biological samples—changes in the optical path length due to expansion of

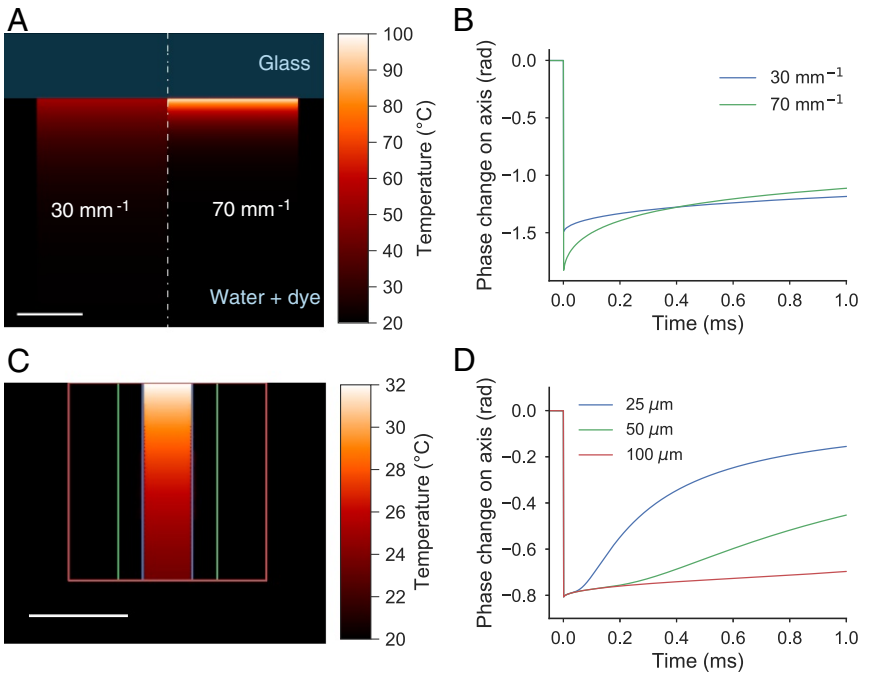

Fig. 5. Phase changes during heating and thermal relaxation. (*A*) Temperature maps for absorption coefficients of 30 mm^{-1} and 70 mm^{-1} at the end of the 1-μs heating pulse. Only half width is shown on each side for compactness. (Scale bar: 50 μm.) (*B*) Phase change along the center of the heating beam. (*C*) Temperature map of the narrowest cylinder at the end of the 1-μs heating pulse. The colored lines represent the outlines of the other cylinders. (Scale bar: 50 μm.) (*D*) Phase changes along the center of the object, assuming the refractive index being that of water. Since the incident radiant exposure (energy per unit area) was kept constant and the pulse duration was shorter than the heat confinement time, the maximum phase change is the same for all three objects. However, the relaxation time course varies with the object size since smaller objects cool down faster.

biological materials are typically around three times larger than those caused by just the variation of refractive index with temperature (9). This difference was demonstrated in our measurements of a thin film heating with QPI and with OCT. With QPI, refractive index change in water precisely accounted for the observed signal. With OCT, however, observed phase changes exceeded the contribution of the refractive index change in water by a factor of 2.4: 0.57 rad could be accounted for by modeling the contribution of water out of 1.34 rad observed. Additionally, the superposition of contributions from multiple depths may complicate the interpretation of phase changes with backscattered light (36).

Imaging thermal changes in the refractive index also enables mapping of the electric current density in a conductive medium. The spatial resolution of the thermal mapping is limited not only by the optical resolution of the phase imaging system, but also by heat diffusion. Therefore, duration of the heating pulse and the image acquisition time should be selected so that the heat diffusion length does not exceed the desired spatial resolution. The heat diffusion time t across a length L can be estimated as $t = L^2/4\alpha$, where α is the thermal diffusivity ($\alpha = 1.4 \times 10^{-3}$ cm^2/s for water). For our pipette with 3.2 μm radius, the characteristic heat diffusion time is $t \sim 18$ μs, which defined our selection of a current pulse duration of 20 μs, while our 1-μs camera exposure time was much shorter. For samples requiring shorter exposures, pump–probe measurements can be performed with even femtosecond pulse durations and delays.

Electric currents or other material property can be retrieved by fitting the model to the experimental phase changes if (*i*) other parameters in the model are known a priori and (*ii*) the phase changes monotonically with the material property of interest. Other than retrieving the current density by gradient descent optimization, the 3D distribution of electric current density could theoretically be reconstructed from a collection of 2D phase maps measured during heating. Since the total phase change corresponds to the integral of the refractive index changes along the imaging axis, tomographic algorithms, such as filtered back projection (37) or back propagation (38), could be used for reconstruction. If the electric current density is not axially symmetric, it can be reconstructed from a collection of 2D phase maps acquired at different projection angles (39); otherwise a single phase map should suffice. Distribution of the electric current density j can then be obtained from an index change map Δn as

$$j(x, y, z) = \sqrt{\frac{c\rho\sigma \cdot \Delta n(x, y, z)}{\frac{dn}{dT} \cdot \Delta T}}, \qquad [6]$$

where c, ρ, and σ are the heat capacity, density, and electrical conductivity of the medium, respectively.

In semiconductors, imaging the dynamics of light-induced or electrically induced changes in refractive index could be used to measure dopant deposition depth or detect the presence of impurities and defects that affect the lifetime of the photo-induced carriers. Techniques based on photo-induced changes in reflectivity at the semiconductor surface are routinely used for measuring dopant concentrations or evaluating surface properties (40, 41). Integration of phase changes deep inside the material with both QPI and OCT can greatly increase the sensitivity of this technique compared with surface-only reflectivity measurements. Depth-resolved mapping with QPI and OCT can also reveal subsurface structures without the need for sample cutting by focused ion beam as required today. In addition, as we demonstrated through modeling, the time course of signal relaxation can provide information about the size and shape of hidden features.

Finally, our results also suggest that phase-resolved OCT can rapidly detect the rate of energy deposition in tissue and could become an all-optical alternative to optoacoustics for mapping

the tissue pigmentation or real-time control of retinal laser therapy (8). It has been shown that Doppler OCT can measure heat-induced motion of retinal tissue (9). However, monitoring phase changes during laser exposures lasting from 50 ms to 400 ms was challenging due to eye movements, which introduce significant motion artifacts over such timescales. We propose instead to measure the temperature rise during the 0.5-ms heating pulse and use this information to define the required power and/or duration of the laser exposure to achieve photocoagulation of the desired clinical grade. For such a short measurement, eye movements and blood pulsation are less likely to affect the signal. In addition, such a short probe can be performed without tissue damage, while using much higher peak power than is used during 20-ms laser therapy. If signal processing requires only a few milliseconds, the treatment pulse can be applied to the same spot right after the probe. If the signal processing will take longer, it might be more efficient to first probe the treatment pattern area with OCT thermometry and then apply the pattern treatment based on the absorption data obtained during the mapping phase. With 45 dB SNR (which commercial systems can readily attain), phase-resolved OCT can detect a temperature rise of 0.5 °C within a 20-μm–thick layer of tissue, thereby providing sufficient precision (1%) even for nondamaging retinal laser treatment, which has a width of the therapeutic window of about 30% (42).

An interesting option for improving the SNR is to use the same laser for thermal treatment and for OCT phase measurements. Since the treatment laser power is about two orders of magnitude higher than that of an OCT beam (typically <1 mW), it would greatly improve the SNR. Additionally, Rayleigh scattering scales with wavelength as λ^{-4}; therefore using the green–yellow wavelengths (530–570 nm) of the treatment beam for imaging instead of near infrared (1,060 nm in our system) would also increase the scattering by more than an order of magnitude. Much stronger retinal scattering would then help better define the location of the retinal surface and the front of the RPE for monitoring tissue expansion between these two layers. Availability of a cost-effective broadband laser suitable for this purpose is uncertain at this point.

Conclusions

Interferometric imaging of transient thermal perturbations with techniques such as QPI and phase-resolved OCT enables precise mapping of the sample properties, such as absorption, conductivity, lifetime of charge carriers in semiconductors, distribution of electric current, and others. With a deep penetrating beam, objects hidden in the bulk can be detected, and the signal relaxation time can reveal their size and shape. We demonstrated that thermal measurements based on changes in refractive index are sensitive to deposition of about 3.4 mJ/cm^2 energy in aqueous samples, corresponding to a subdegree temperature increase in single cells. Temporal resolution in pulse–probe experiments is limited only by the duration of the illumination flash. QPI is relatively insensitive to thermal expansion of the samples, but with OCT, refractive index changes and sample expansion both contribute to changes in the optical path length, with the latter being the dominant source of signal in polymers and biological tissues. Phase-resolved OCT can be used to measure heat-induced changes in RPE and choroid, which may enable accurate titration of the energy deposition for retinal laser therapy.

Materials and Methods

High-Speed Quantitative Phase Imaging. Wide-field measurements of thermally induced changes in refractive index were performed using high-speed diffraction phase microscopy (35). The collimated, bandpass-filtered (715–950 nm; Semrock filters FF01-715/LP-25 and FF01-950/SP-25) beam of a supercontinuum laser (Fianium SC-400-4; NKT Photonics) was used to illuminate transparent samples on an inverted microscope (Eclipse TE-2000; Nikon) (Fig. 6*A*). Using a 10× objective (CFI HMC 10×, N.A. 0.25; WD 6.2 mm; Nikon) and a 200-mm tube lens (Nikon), images were projected onto a linear amplitude diffraction grating (110 lines per millimeter; Edmund Optics). A spatial filtering system was built using lenses of 50 mm (AF Nikkor 50 mm f/1.8D; Nikon) and 250 mm (LB1889-B; Thorlabs) in a 4f configuration, with the spatial filter positioned in the focal plane of the first lens. A reference beam was created by spatially filtering the 0th diffraction order of the grating through a 150-μm pinhole. The first diffraction order passed unaffected through a rectangular window, while higher diffraction orders were blocked. The beams recombined on a camera, forming an overlay of the sample image with a linear diffraction pattern defined by the off-axis incidence of the first-order beam. With an equivalent sample irradiance of 43 mW/mm^2 from an 830-nm source, exposures could be as short as 1 μs for transparent samples. With a Vision Research v641 high-speed camera, the frame rate could reach 53,900 fps with a resolution of 256 × 128 pixels.

To describe the interference pattern on the camera, let I_s denote the intensity of the first diffraction order, which carries the sample phase information; I_r be the reference beam intensity propagating through the pinhole; k be the linear phase tilt introduced by the grating; I be the identity transform; and $\mathcal{F}$ be the low-pass filter operation of the pinhole. Then, the interference pattern on the camera can be described as follows (43):

$$I(\mathbf{x}, t) = I_s(\mathbf{x}, t) + I_r(t) + 2\sqrt{I_s I_r}\cos\left(\mathbf{k}\cdot\mathbf{x} + (\mathcal{I} - \mathcal{F})[\Phi_s(\mathbf{x}, t)]\right). \quad [7]$$

The phase map of the sample $\Phi_s^{(est)}(\mathbf{x}, t)$ can be obtained from these data following a technique previously described in the literature (44). Briefly, a Fourier transform of the sample under study ("sample") and of a reference image ("reference") is first obtained. For both the sample and the reference, the first diffraction order was centered and isolated with a low-pass filter, and the inverse Fourier transform of the resulting images was calculated. The resulting phase maps are the complex angle of the pointwise division of the final reference and sample (complex) images.

Phase-Resolved OCT. The phase-stabilized swept-source OCT was assembled following a layout previously described in the literature (45). The high-speed swept-source laser (Axsun Technologies 1,060-nm swept laser) had a center wavelength of 1,060 nm and a usable bandwidth of 110 nm. The wavelength was swept from short to long wavelengths at a 100-kHz repetition rate with a nearly 50% duty cycle, and the average output power was 15 mW.

The output laser beam, coupled into a fiber-based interferometer, was collimated (C_1, f = 11.0 mm, PAF-X-11-B; Thorlabs) and split between the reference and sample beams using a 90:10 (R:T) beam splitter (BS029; Thorlabs), as shown in Fig. 6*C*. The beam was projected onto the sample using a 60-mm achromatic doublet lens (ACA254-060-B; Thorlabs), forming a 40-μm spot in the focal plane. Backscattered light was collected by a large aperture collimator (C_3, f = 18.4 mm, PAF-X-18-B; Thorlabs). Lateral position of the OCT probe on the sample was controlled by a tip–tilt mirror (M_2, S-334; Physik Instrumente). The reference beam was coupled (C_2, f = 11.0 mm, PAF-X-11-B; Thorlabs) into the fiber. Ten percent of the light in the reference arm was sent into a MZI to measure the nonlinear wavenumber sampling by the swept-source laser. The remaining 90% of the light was delivered to an air gap, where the chromatic dispersion of the sample arm optics was matched. An iris in this part of the beam path controlled the amount of light reaching the detector. The sample and reference arms were recombined using a 50/50 fiber coupler, and the signal was detected on a balanced photoreceiver (PDB480C-AC; Thorlabs). In the MZI, light split into two arms using a 75/25 fiber coupler passed through an air gap before the beams were recombined with a 50/50 fiber coupler, and signal was measured on a balanced photoreceiver (PDB480C-AC; Thorlabs). The air gaps were mismatched by 1.6 mm to create a 31.4-MHz signal. An AlazarTech ATS9350 dual-channel data-acquisition (DAQ) card (Alazar Technologies) was used for recording and for synchronization of the A-scan acquisition with the heating laser. Acquired interference fringes had to be corrected for nonlinear sampling of the wavenumber by the acquisition system, which we performed using the MZI signal, following the method in ref. 45. Numerical dispersion compensation after wavenumber resampling was performed by applying a static transformation to every A-scan obtained by imaging a specular reflection off a mirror placed in the focal plane of the sample arm (46–48).

Relative phase changes $\Delta\phi$ in the backscattered light from two different depths within a single A-scan (depth profile) were obtained as a result of the relative translation of the reflection planes by a distance δ through the equation $\Delta\phi = 2n\langle k\rangle\delta$, where n is the refractive index, and $\langle k\rangle$ is the average wavenumber of the OCT source (15, 49).

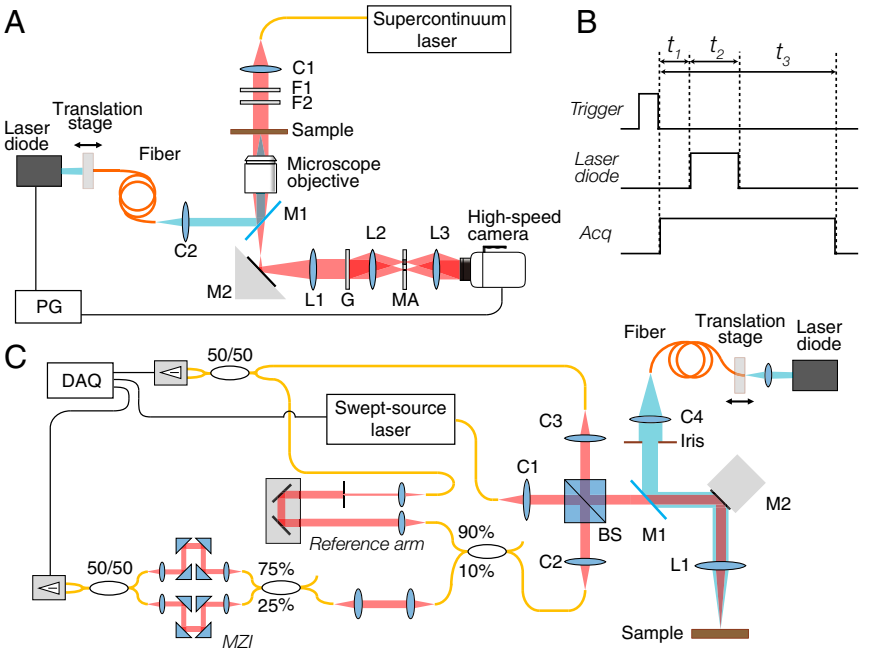

Fig. 6. Optical layouts. (*A*) QPI microscope. Collimated (C1) and band-pass–filtered (F1, F2) light from a supercontinuum laser illuminates a sample; a microscope objective and tube lens L1 project the image onto a grating (G). A 4f system (L2, L3) with filters (MA) creates an interferogram of the 0th and first diffraction orders on a high-speed camera. A heating blue laser is delivered to the sample from a multimode fiber via a relay lens (C2) and a dichroic mirror. (*B*) Trigger and heating laser pulses are generated by the pulse generator (PG), while the imaging system controls the acquisition duration directly. (*C*) For the phase-resolved OCT, light from a swept-source laser is split into a reference and a sample arm. The heating beam is aligned collinear with the probing OCT beam by a dichroic mirror, and both arms are focused at the same height onto the sample. In the reference arm, 10% of the light is sent into a Mach–Zender interferometer (MZI) for numerical compensation for nonuniform wavenumber sampling by the swept-source laser. The other 90% of the light is delivered to an air gap where dispersion of the sample arm is matched (middle), and the resulting light is recombined with the backscattered sample arm to obtain the OCT signal.

Samples Imaged in QPI. Transient thermal changes in two different samples were imaged with the QPI microscope. The first one consisted of a 3-μm–thick red film painted on a 1-mm–thick glass slide and heated by a pulse of blue (450 nm) laser (Fig. 6*A*). Light from a 200-μm multimode fiber was projected onto a 25-μm spot of uniform intensity on the red film, using a 150-mm relay lens (LB1374-A; Thorlabs) and a 10× microscope objective. A long-pass dichroic mirror was used to couple the blue beam into the QPI path. The film absorbed 60% of the incident energy. Timing of the heating pulses was controlled with an SRS DG535 digital pulse generator, synchronized with the v641 camera (Fig. 6*B*). The acquisition frame rate was 10,800 Hz, with 10-μs exposures.

In a second experiment, we imaged pulsed heating of the electrolyte by electric current injected into the medium via a glass pipette with a 10-μm exterior and 6.4-μm interior tip diameter. The electrolyte consisted of 50 g NaCl and 150 g glucose dissolved in 200 mL distilled water, and its conductivity was 14 S/m. Glucose was used to better match the electrolyte refractive index to the glass of the pipette. The pipette impedance was 40 kΩ, and 20-μs–long, 0.9-mA square pulses of current were delivered from a current pulse generator (Model 2100; AM Systems) to an electrode inside the pipette, with the return electrode in the Petri dish. For this measurement, the camera frame rate was 50,000 Hz with 1-μs exposure time, and the camera clock was externally synchronized with the pulse generator to capture the interferogram during the last 1 μs of the electrical pulse.

Samples Imaged with OCT. To demonstrate imaging of the thermal response with the phase-resolved OCT system, we first used inorganic samples. One consisted of a 1-mm–thick layer of water stained with a red dye (Alizarin Red S, 21.2 mg/mL, absorption coefficient of 49.4 mm^{-1} at 450 nm) trapped between two 200-μm–thick glass coverslips. The sidewalls of this cuvette were left open to allow for water expansion (Fig. 3*A*). An iris illuminated with 450 nm laser light was imaged onto the glass–water interface, producing a 200-μm diameter spot 400 μm below the surface. The beam diameter was 254 μm on the glass–water interface. The heating beam power was 400 mW, and the pulse duration varied from 0.1 ms to 10 ms. The second sample was a thin (<10 μm) layer of paint (68% absorption at 450 nm) applied on top of a frosted glass slide placed at the bottom of the cuvette filled with water.

We also conducted experiments with the eyecups of Long Evans rats, which included the RPE, choroid, and sclera (n = 3). All experimental procedures were conducted in accordance with the Stanford University Administrative Panel on Laboratory Animal Care and conformed to the guidelines of the Association for Research in Vision and Ophthalmology (ARVO) Statement for the Use of Animals in Ophthalmic and Vision Research. Briefly, after euthanasia, eyes were enucleated and immersed in Ames' medium (Sigma-Aldrich). Eyecups containing the RPE, choroid, and sclera were prepared by hemisecting the eye and removing the anterior segment, lens, and vitreous. Eyecups were flattened by four radial incisions, from the edge to the equator, resulting in four petal-shaped sections. The detached neural retina was gently removed while making sure the RPE cells remained attached to the eyecups. The sample was pinned to a small Petri dish and maintained in fresh Ames' medium during the measurement. The same optical system as described above (450 nm light focused into a 200-μm spot for heating, peak power varying between 62 mW and 500 mW, pulse duration varying between 1 ms and 5 ms, and a 40-μm–wide OCT beam at 1,060 nm for recording) was used, with timing of the heating pulses and acquisition on the DAQ card controlled by an SRS DG535 pulse generator (Stanford Research Systems). For assessment of the measurement reproducibility, 16 spots (4 × 4 grid) were sequentially applied over each petal-shaped section of the eyecup, at the same power level within the section.

Modeling Thermally Induced Phase Changes. We modeled the thermal effects of energy deposition into our samples by light and by electric current, using FEM software (COMSOL). All samples were assumed to be axially symmetric (see Dataset S1 for a sample model file), and temperature was calculated by solving the heat-diffusion equation

$$\rho c_p \frac{\partial T}{\partial t} = \nabla\,(k\nabla T) + Q(r, z, t), \qquad [8]$$

where ρ is the density of the sample, c_p is the heat capacity, k is the thermal conductivity, and Q is the volumetric heat source. The initial temperature

for all models was 20 °C. With laser heating, we modeled the heat source using the Beer–Lambert law

$$Q(r, z, t) = \mu(z) \cdot \phi(r, t) \cdot e^{-\mu(z) \cdot z}, \quad [9]$$

where $\mu(z)$ is the absorption coefficient, and $\phi(r, t)$ the incident beam profile is assumed to be top hat, unless otherwise specified. Absorption coefficients were set based on the measurements of the total absorption and sample thickness.

For modeling heating by electric current, we captured the pipette geometry from photographs, constrained the input voltage into the pipette to match the applied current, and obtained the resulting distribution of the current density in the electrolyte of known conductivity. Finally, the Joule heat source term was coupled into the heat-diffusion equation. After solving for the evolution of temperature, we estimated the changes in the refractive index of water using the relationship in Table S1 (50).

In addition to changes in the refractive index of water, for some samples, we also modeled thermal expansion of glass using a linear expansion coefficient of 5.22×10^{-6} K^{-1} chosen to match the experimentally measured phase change. This coefficient is within the range of linear thermal expansion coefficients of ordinary glass, $3.2–8.5 \times 10^{-6}$ K^{-1} reported in the literature.

Retrieval of Material Properties by Gradient Descent. Retrieval of material properties such as absorption coefficient, diameter of the heated object, or current density from the phase change measured by QPI or OCT can be performed using optimization techniques. The material property α is found by minimizing a cost function $E(\alpha)$, which represents the difference between the experimental and modeling results, integrated over the measured time course

$$E(\alpha) = \sum_{i=0}^{N} [\phi(t_i; \alpha) - \phi(t_i)]^2, \quad [10]$$

where $\phi(t_i; \alpha)$ is the phase change calculated by the model with the approximation α, and $\phi(t_i)$ is the experimental phase change at the same instant in time t_i. Since the phase changes monotonically with temperature, as well as thermal relaxation time scales monotonically with the object diameter (Fig. 5), these properties can be reconstructed by minimizing the cost function $E(\alpha)$. One way of solving this optimization problem uses the gradient descent method, converging from the initial guess of $\alpha^{(0)}$ to a close approximation of the true value of α by iterations

$$\alpha^{(n)} = \alpha^{(n-1)} - \tau \cdot \nabla E(\alpha^{(n-1)}), \quad [11]$$

where τ is the step size for optimization. The optimization procedure is stopped when the differences between the modeled and experimental time courses decrease to the noise level.

Laser Damage Threshold Determination for RPE. A live/dead fluorescent assay was performed to assess RPE cell damage after laser exposure using a viability/cytotoxicity assay kit (Biotium). In this kit, Calcein AM produces green fluorescence in viable cells and Ethidium Homodimer III penetrates to the nuclei and emits red fluorescence upon binding to DNA in dead cells. After laser treatment, samples were incubated in the dye solution for 30 min at room temperature, washed with PBS three times, and then imaged under a fluorescent microscope. The damage threshold was defined as the transition from live to dead cells between patterns with 10% power increments.

Estimating Laser-Induced Temperature Rise in the RPE. We used FEM software (COMSOL) to assess the temperature. Parameters of the retinal heating model for 532-nm and 577-nm wavelengths (42, 51, 52) were adapted for the 450-nm laser by adjusting the absorption of melanin (53) and scattering of biological tissue (26), as is shown in Table S2. Thermal conductivity and heat capacity of the tissue were set to 0.54 W/(m K) and 3,735 J/(kg K), respectively. For more precise calibration of the absorption coefficients, we calculated the Arrhenius damage integral as

$$\Omega(\tau) = A \int_0^{\tau} e^{-\frac{E^*}{R \cdot T(t)}} dt, \quad [12]$$

where $E^* = 340$ kJ·mol^{-1}, $A = 1.6 \times 10^{55}$ s^{-1}, and $R = 8.3145$ J·mol^{-1}·K^{-1}. We adjusted the absorption coefficient of melanin to ensure that $\Omega = 1$ for the power levels corresponding to the experimental damage thresholds at 1-ms pulse duration. As a control, we then verified that it matched the damage threshold at 5-ms pulse duration.

ACKNOWLEDGMENTS. We thank Dr. A. Roorda and Dr. F. LaRocca for helpful comments and encouragement, Christine Cordeiro for providing support for the QPI microscope, and Dr. Henri Lorach for OCT imaging of the ocular tissue. Funding was provided by the US National Institutes of Health (National Eye Institute Grants U01-EY025501 and P30-EY026877) and an unrestricted grant from Research to Prevent Blindness. G.G. was supported by a Stanford Neurosciences Institute interdisciplinary scholarship.

1. Vavilov VP, Maldague X, Dufort B, Robitaille F, Picard J (1993) Thermal nondestructive testing of carbon epoxy composites: Detailed analysis and data processing. *NDT E Int* 26:85–95.
2. Maldague X (2001) *Theory and Practice of Infrared Technology for Nondestructive Testing, Wiley Series in Optical and Microwave Engineering* (Wiley, Hoboken, NJ).
3. Vavilov VP, Burleigh DD (2015) Review of pulsed thermal NDT: Physical principles, theory and data processing. *NDT E Int* 73:28–52.
4. Toivanen JM, et al. (2014) 3D thermal tomography with experimental measurement data. *Int J Heat Mass Transf* 78:1126–1134.
5. Poudel A, Shrestha SS, Sandhu JS, Chu TP, Pergantis CG (2015) Comparison and analysis of acoustography with other NDE techniques for foreign object inclusion detection in graphite epoxy composites. *Compos B Eng* 78:86–94.
6. Yurt A, Unlu S, Goldberg B, Ramsay E (2015) Dual-phase interferometry for charge modulation mapping in ICS. US Patent Appl 14/433,732.
7. Yamaguchi M, Ito A, Ono A, Kawabe Y, Kamihira M (2014) Heat-inducible gene expression system by applying alternating magnetic field to magnetic nanoparticles. *ACS Synth Biol* 3:273–279.
8. Brinkmann R, et al. (2012) Real-time temperature determination during retinal photocoagulation on patients. *J Biomed Opt* 17:061219.
9. Muller HH, et al. (2012) Imaging thermal expansion and retinal tissue changes during photocoagulation by high speed OCT. *Biomed Opt Express* 3:1025–1046.
10. Kaiplavil S, Mandelis A (2014) Truncated-correlation photothermal coherence tomography for deep subsurface analysis. *Nat Photonics* 8:635–642.
11. Romano M, Sommier A, Batsale JC, Pradere C (2016) 3D transient temperature measurement in homogeneous solid material with THz waves. *Proc SPIE* 9896: 98960K.
12. Arab S, Yao M, Zhou C, Daniel Dapkus P, Cronin SB (2016) Doping concentration dependence of the photoluminescence spectra of n-type GaAs nanowires. *Appl Phys Lett* 108:182106.
13. Itzkan I, et al. (1995) The thermoelastic basis of short pulsed laser ablation of biological tissue. *Proc Natl Acad Sci USA* 92:1960–1964.
14. Hyle Park B, et al. (2005) Real-time fiber-based multi-functional spectral-domain optical coherence tomography at 1.3 μm. *Opt Express* 13:3931–3944.
15. Joo C, Akkin T, Cense B, Park BH, De Boer JF (2005) Spectral-domain optical coherence phase microscopy for quantitative phase-contrast imaging. *Opt Lett* 30:2131–2133.
16. Adler DC, Huang SW, Huber R, Fujimoto JG (2008) Photothermal detection of gold nanoparticles using phase-sensitive optical coherence tomography. *Opt Express* 16:4376–4393.
17. Boyer D, Tamarat P, Maali A, Lounis B, Orrit M (2002) Photothermal imaging of nanometer-sized metal particles among scatterers. *Science* 297:1160–1163.
18. Vermeulen P, Cognet L, Lounis B (2014) Photothermal microscopy: Optical detection of small absorbers in scattering environments. *J Microsc* 254:115–121.
19. Shaked NT, Newpher TM, Ehlers MD, Wax A (2010) Parallel on-axis holographic phase microscopy of biological cells and unicellular microorganism dynamics. *Appl Opt* 49:2872–2878.
20. Miccio L, et al. (2011) Dynamic DIC by digital holography microscopy for enhancing phase-contrast visualization. *Biomed Opt Express* 2:331–344.
21. Edwards C, et al. (2014) Diffraction phase microscopy: Monitoring nanoscale dynamics in materials science invited. *Appl Opt* 53:G33–G43.
22. Chowdhury S, Eldridge WJ, Wax A, Izatt JA (2015) Spatial frequency-domain multiplexed microscopy for simultaneous, single-camera, one-shot, fluorescent, and quantitative-phase imaging. *Opt Lett* 40:4839–4842.
23. Evans AA, Bhaduri B, Popescu G, Levine AJ (2017) Geometric localization of thermal fluctuations in red blood cells. *Proc Natl Acad Sci USA* 114:2865–2870.
24. Kandel ME, Teng KW, Selvin PR, Popescu G (2017) Label-free imaging of single microtubule dynamics using spatial light interference microscopy. *ACS Nano* 11:647–655.
25. Cordeiro C, et al. (2017) Optophysiology of cardiomyocytes: Characterizing cellular motion with quantitative phase imaging. *Biomed Opt Express* 8:4652–4662.
26. Jacques SL (2013) Optical properties of biological tissues: A review. *Phys Med Biol* 58:R37–R61.
27. Mourant JR, et al. (1998) Mechanisms of light scattering from biological cells relevant to noninvasive optical-tissue diagnostics. *Appl Opt* 37:3586–3593.
28. Cone MT, et al. (2015) Measuring the absorption coefficient of biological materials using integrating cavity ring-down spectroscopy. *Optica* 2:162–168.
29. Hosseini P, et al. (2016) Pushing phase and amplitude sensitivity limits in interferometric microscopy. *Opt Lett* 41:1656–1659.
30. De Boer JF, et al. (2003) Improved signal-to-noise ratio in spectral-domain compared with time-domain optical coherence tomography. *Opt Lett* 28:2067–2069.
31. Kell GS (1975) Density, thermal expansivity, and compressibility of liquid water from 0.deg. to 150.deg.. Correlations and tables for atmospheric pressure and saturation reviewed and expressed on 1968 temperature scale. *J Chem Eng Data* 20:97–105.

32. Schmidt SY, Peisch RD (1986) Melanin concentration in normal human retinal pigment epithelium. Regional variation and age-related reduction. *Invest Ophthalmol Vis Sci* 27:1063–1067.
33. Hillmann D, et al. (2016) In vivo optical imaging of physiological responses to photostimulation in human photoreceptors. *Proc Natl Acad Sci USA* 113:13138–13143.
34. White BR, et al. (2003) In vivo dynamic human retinal blood flow imaging using ultra-high-speed spectral domain optical Doppler tomography. *Opt Express* 11:3490–3497.
35. Popescu G, Ikeda T, Dasari RR, Feld MS (2006) Diffraction phase microscopy for quantifying cell structure and dynamics. *Opt Lett* 31:775–777.
36. Hu C, Popescu G (2017) Physical significance of backscattering phase measurements. *Opt Lett* 42:4643–4646.
37. Kak AC, Slaney M (1988) *Principles of Computerized Tomographic Imaging* (IEEE, New York).
38. Wedberg T, Stamnes J, Singer W (1995) Comparison of the filtered backpropagation and the filtered backprojection algorithms for quantitative tomography. *Appl Opt* 43:6575–6581.
39. Choi W, et al. (2007) Tomographic phase microscopy. *Nat Methods* 4:717–719.
40. Esser A, Maidorn G, Kurz H (1992) Semiconductors and semimetals. *Appl Surf Sci* 94:482–489.
41. Manolatou C, Lipson M (2006) All-optical silicon modulators based on carrier injection by two-photon absorption. *J Lightwave Technol* 24:1433–1439.
42. Lavinsky D, et al. (2016) Nondamaging retinal laser therapy: Rationale and applications to the macula. *Invest Ophthalmol Vis Sci* 57:2488–2500.
43. Bhaduri B, et al. (2014) Diffraction phase microscopy: Principles and applications in materials and life sciences. *Adv Opt Photonics* 6:57–119.
44. Pham HV, Edwards C, Goddard LL, Popescu G (2013) Fast phase reconstruction in white light diffraction phase microscopy. *Appl Opt* 52:A97–A101.
45. Braaf B, et al. (2011) Phase-stabilized optical frequency domain imaging at 1-μm for the measurement of blood flow in the human choroid. *Opt Express* 19:20886–20903.
46. de Boer JF, Saxer CE, Nelson JS (2001) Stable carrier generation and phase-resolved digital data processing in optical coherence tomography. *Appl Opt* 40:5787–5790.
47. Wojtkowski M, et al. (2004) Ultrahigh-resolution, high-speed, Fourier domain optical coherence tomography and methods for dispersion compensation. *Opt Express* 12:2404–2422.
48. Cense B, et al. (2004) Ultrahigh-resolution high-speed retinal imaging using spectral-domain optical coherence tomography. *Opt Express* 12:2435–2447.
49. Vakoc BJ, Yun SH, De Boer JF, Tearney GJ, Bouma BE (2005) Phase-resolved optical frequency domain imaging. *Opt Express* 13:5483–5493.
50. Schiebener P, Straub J, Sengers JMHL, Gallagher JS (1990) Refractive index of water and steam as function of wavelength, temperature and density. *J Phys Chem Ref Data* 19:677–717.
51. Sramek C, et al. (2009) Dynamics of retinal photocoagulation and rupture. *J Biomed Opt* 14:034007.
52. Wang J, Quan Y, Dalal R, Palanker D (2017) Comparison of continuous-wave and micropulse modulation in retinal laser therapy. *Invest Ophthalmol Vis Sci* 58:4722–4732.
53. Kollias N (1995) The spectroscopy of human melanin pigmentation. *Melanin: Its Role in Human Photoprotection*, eds Zeise L, Chedekel MR, Fitzpatrick TB (Valdenmar Publishing, Overland Park, KS), pp 31–38.